

Properties and Origins of the Anisotropic Eddy-Induced Transport in the North Atlantic

IGOR KAMENKOVICH

Rosenstiel School of Marine and Atmospheric Science, University of Miami, Miami, Florida

IRINA I. RYPINA

Woods Hole Oceanographic Institution, Woods Hole, Massachusetts

PAVEL BERLOFF

Department of Mathematics and Grantham Institute for Climate Change, Imperial College London, London, United Kingdom

(Manuscript received 13 August 2014, in final form 10 December 2014)

ABSTRACT

This study examines anisotropic transport properties of the eddying North Atlantic flow, using an idealized model of the double-gyre oceanic circulation and altimetry-derived velocities. The material transport by the time-dependent flow (quantified by the eddy diffusivity tensor) varies geographically and is anisotropic, that is, it has a well-defined direction of the maximum transport. One component of the time-dependent flow, zonally elongated large-scale transients, is particularly important for the anisotropy, as it corresponds to primarily zonal material transport and long correlation time scales. The importance of these large-scale zonal transients in the material distribution is further confirmed with simulations of idealized color dye tracers, which has implications for parameterizations of the eddy transport in non-eddy-resolving models.

1. Introduction

There is growing evidence for the importance of eddies—defined here as geostrophic deviations from a mean state—in the distribution of various oceanic tracers in the interior of oceanic gyres. In particular, eddies have been shown to maintain the Northern Hemisphere thermocline (e.g., [Henning and Vallis 2004](#)) and to control the penetration of transient atmospheric gases into the North Atlantic (e.g., [Booth and Kamenkovich 2008](#)). The efficiency of eddies in downgradient tracer transport has been conventionally quantified by turbulent (“eddy”) diffusivity. Under the assumptions of homogeneous and isotropic turbulence, the diffusivity K can be related to the rms Lagrangian velocity $\langle v' \rangle$ of tracer particles and the Lagrangian correlation length scale l_{corr} or time scale τ_{corr} ([Taylor 1921](#); [Vallis 2006](#)):

$$K \sim \langle v' \rangle l_{\text{corr}} \sim \langle v' \rangle^2 \tau_{\text{corr}}. \quad (1)$$

In the Eulerian analog of the above equation, the $\langle v' \rangle^2$ becomes the eddy kinetic energy (EKE): the Eulerian mixing length l_{corr} and the Eulerian time scale τ_{corr} ([Prandtl 1925](#)). The eddy diffusivity and other parameters in (1) can be estimated in observational data and numerical simulations by a variety of techniques. Such estimates have practical importance, as diffusion is widely used to parameterize eddies in non-eddy-resolving numerical models, which still account for the majority of ocean components of climate models. The diffusivities in these models are poorly constrained and determined empirically and are often taken to be spatially homogeneous and isotropic.

Existing evidence based on observational estimates and numerical simulations, however, suggests that the eddy-induced transport is spatially inhomogeneous (e.g., [LaCasce and Bower 2000](#)) and anisotropic, that is, it has a preferred direction (e.g., [Freeland et al. 1975](#); [Spall et al. 1993](#); [LaCasce 2000](#)). The along-isopycnal eddy diffusivity can be described by a location-dependent two-dimensional tensor, and the preferred direction can be determined by diagonalizing this tensor. The latter approach was taken by [Rypina et al. \(2012\)](#), who analyzed trajectories of both

Corresponding author address: Igor Kamenkovich, 4600 Rickenbacker Causeway, University of Miami, Miami, FL 33149.
E-mail: ikamenkovich@rsmas.miami.edu

synthetic Lagrangian particles (diagnosed from the altimetric data) and the actual surface drifters in the North Atlantic. The results demonstrate that the preferred transport direction varies across the region, the transport anisotropy is caused primarily by geostrophic rather than nongeostrophic currents (see also Sallee et al. 2008), and the spreading of Lagrangian particles can be faster or slower than diffusive, that is, “superdiffusive” or “subdiffusive,” respectively (see also Berloff et al. 2002; Veneziani et al. 2005; Kamenkovich et al. 2009).

The origins of this complexity remain largely unclear, and several mechanisms have been proposed. The mean advection can significantly modulate the eddy-induced transport. In particular, the meridional diffusivity is enhanced at steering levels (Green 1970; Killworth 1997) and is suppressed by zonal propagation of eddies relative to the mean zonal flow (Ferrari and Nikurashin 2010); meridional shear in zonal currents can cause shear dispersion (e.g., Taylor 1953; Young et al. 1982; Smith 2005); and cross-jet transport barriers exist on strong currents such as the Gulf Stream and its extension (Samelson 1992; Rypina et al. 2011) and alternating multiple jets (Haynes et al. 2007; Berloff et al. 2009). In addition, powerful mean currents, such as those within the western boundary regions and the upper-ocean Antarctic Circumpolar Current, can dwarf the along-stream eddy-induced transport.

In many parts of the ocean, however, mean currents are weak relative to eddies, and the along-stream diffusivity is as important for tracer distribution as the mean advection. In these regions, the anisotropy cannot be explained by the effects of the mean advection alone (Kamenkovich et al. 2009; Rypina et al. 2012). On the other hand, the eddy velocity variance tends to be isotropic (Rypina et al. 2012) and cannot explain anisotropy in K using (1) either. Kamenkovich et al. (2009) hypothesize that the dominance of the zonal eddy diffusivity can be caused by zonally elongated eddies such as those observed in altimetry-based observational datasets (Huang et al. 2007), and this hypothesis is further examined in this study. This manuscript investigates the influence of zonally elongated transient patterns on the particle spreading, describes spectral and transport properties of these transients in idealized numerical simulations (sections 2 and 3) and altimetry-based velocity estimates (section 4), and discusses the importance of transient motions in idealized tracer distribution in the model context in section 5.

2. Numerical model and simulated flow

The dynamical model is adapted from Karabasov et al. (2009) and only a very brief description of it is given here. This model employs an advanced advection scheme Compact Accurately Boundary-Adjusting High-Resolution

Technique (CABARET) which allows achieving highly effective spatial resolution, meaning that numerical convergence is found at much coarser spatial resolution than in the case of traditional advection schemes. An equally important and attractive property of this formulation is its numerical stability in the presence of small dissipation, which allows simulations with very high, and most realistic, Reynolds numbers (Re).

The vertical stratification is represented by three isopycnal layers, with the thicknesses of 250, 750, and 3000 m, counting from the top. The evolution of the potential vorticity (PV) q_n in each layer is described by

$$\frac{\partial q_n}{\partial t} + \mathbf{J}(\psi_n, q_n) = \nu \nabla^4 \psi_n + \mathcal{F}_n, \quad n = 1, 2, 3, \quad (2)$$

where the lateral Laplacian viscosity ν is $100 \text{ m}^2 \text{ s}^{-1}$. This value has been chosen to correspond to the Munk boundary layer of 17 km that is minimally resolved with two grid points. PV in each layer is given by

$$\begin{aligned} q_1 &= \beta y + \nabla^2 \psi_1 - \frac{1}{R_1^2} (\psi_1 - \psi_2) \\ q_2 &= \beta y + \nabla^2 \psi_2 - \frac{1}{R_{21}^2} (\psi_2 - \psi_1) - \frac{1}{R_{22}^2} (\psi_2 - \psi_3) \\ q_3 &= \beta y + \nabla^2 \psi_3 - \frac{1}{R_3^2} (\psi_3 - \psi_2), \end{aligned} \quad (3)$$

where the stratification parameters R_1 , R_{21} , R_{22} , and R_3 are chosen so that the first and the second internal deformation radii are $R_{d1} = 32.2$ and $R_{d2} = 18.9 \text{ km}$, respectively: $\beta = 2 \times 10^{-11} \text{ m}^{-1} \text{ s}^{-1}$.

The forcing \mathcal{F}_n on the right-hand side of (4) includes Ekman pumping by the prescribed wind stress curl in the top layer and bottom friction in the bottom layer:

$$\begin{aligned} \mathcal{F}_1 &= f_{\text{wind}} \\ \mathcal{F}_2 &= 0 \\ \mathcal{F}_3 &= k_{\text{bot}} \nabla^2 \psi_3, \end{aligned} \quad (4)$$

where f_{wind} is idealized wind forcing, which has a zero curl line slanted in the meridional direction. Bottom friction $k_{\text{bot}} = 10^{-7}$. The domain is square and has a size of 3840 km, and the spatial resolution is 7.5 km.

The simulated flow and its spectrum

The simulated flow consists of subtropical and subpolar gyres, separated by a well-pronounced western boundary current and its eastward jet extension (EJE hereinafter; Fig. 1a). The entire domain is filled with mesoscale eddies, which are particularly strong in the vicinity of the EJE (Fig. 1b). The magnitudes of motions decrease with depth. The spatial structure of the PV is qualitatively

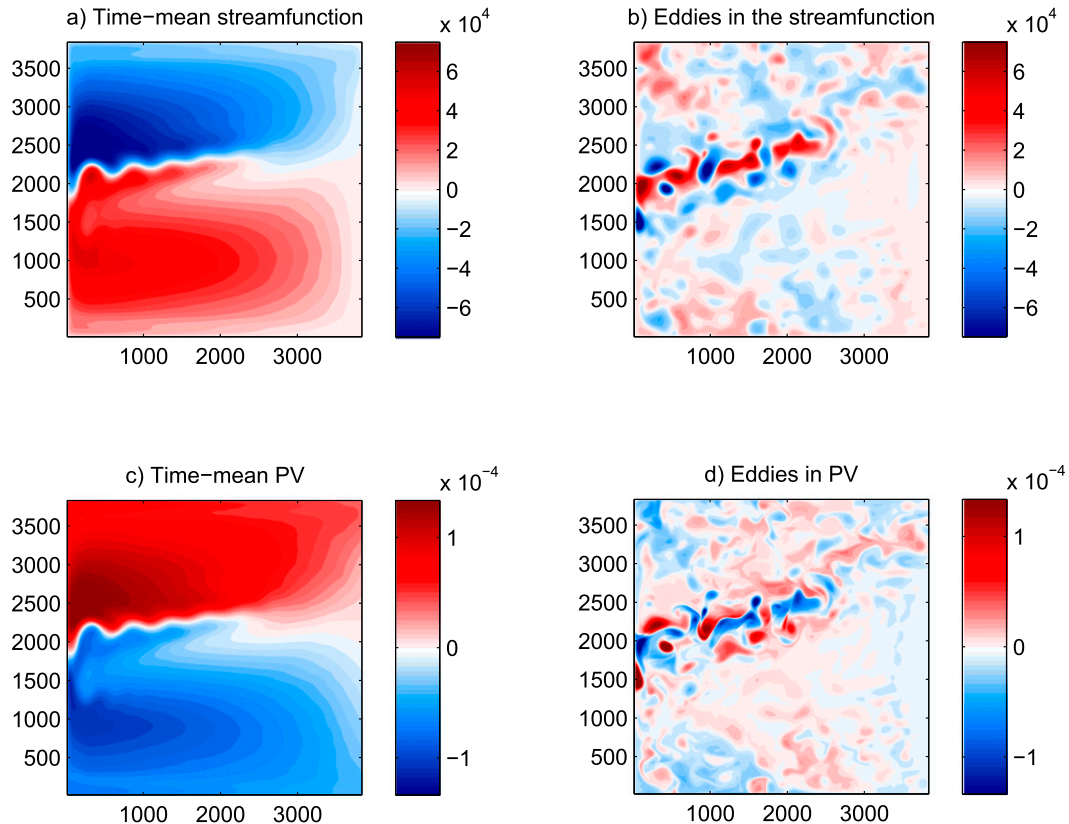


FIG. 1. Circulation in the top layer of the numerical simulations. (a) Time-mean (over 50 yr) streamfunction and (b) instantaneous minus the time-mean streamfunction (eddies) ($\text{m}^2 \text{s}^{-1}$). (c) Time-mean (over 50 yr) PV; (b) instantaneous minus the time-mean PV (eddies) (s^{-1}).

similar to the streamfunction (Figs. 1c,d). This similarity is explained by the dominance of the stretching terms [last terms in (3)], which is because the dominant length scales in the solutions are several Rossby deformation radii (see the following discussion of Fig. 2).

The spatial structure of the eddy field is illustrated by the two-dimensional wavenumber ($k-l$) spectrum of the velocity—the sum of u and v velocity spectra (Fig. 2a). The 2800 spectra of instantaneous velocities are computed at 7-day intervals and then averaged in time; note that these instantaneous $k-l$ spectra do not contain information on time dependence and eddy propagation. Most of the spectral power is contained in the circular band corresponding to the total wavenumbers ($k^2 + l^2$) $^{1/2}$ between $(20R_{d1})^{-1}$ and $(10R_{d1})^{-1}$. Within this spectral region in layer 1, there is a noticeable peak corresponding to the zonal wavelength $k^{-1} = 120R_{d1}$ (total basin width) and the meridional wavelength of $l^{-1} = 13R_{d1}$. This peak corresponds to a nearly meridional wavenumber (Fig. 2b) and is anisotropic in this sense. This anisotropic peak is separated from a second, broader, and bigger peak centered at the 30° orientation of the wavevector. The entire spectral region at $k^{-1} > 30R_{d1}$ will be referred to as the

region of “zonal transients” to distinguish it from more isotropic flow components with shorter zonal scales, which will be loosely referred to as “isotropic eddies.” The zonal transient part of the spectrum corresponds to a relatively small portion of the total energy (e.g., 15% in layer 1); however, we will later see that the zonal transients play an important role in the anisotropic transport. Note that zonal transients are defined in terms of the zonal scales only and not based on dynamical properties. The separation between the two spectral peaks becomes less distinct in layers 2 and 3 (not shown).

To study the meridional structure and propagation properties of zonal transients, we isolate them by spatial filtering of the velocity streamfunction; the filtering is done in the zonal direction only, and the cutoff wavelength is $30R_{d1}$. As the rest of the flow, the zonal transients have maximum amplitudes in the EJE vicinity (Figs. 2c,d). With depth, the distribution of the kinetic energy of the zonal transients becomes more uniform in the meridional direction and the relative importance of zonal transients in the regions north and south of EJE is the largest in layer 3. We will later see that this deep region also corresponds to the largest transport anisotropy.

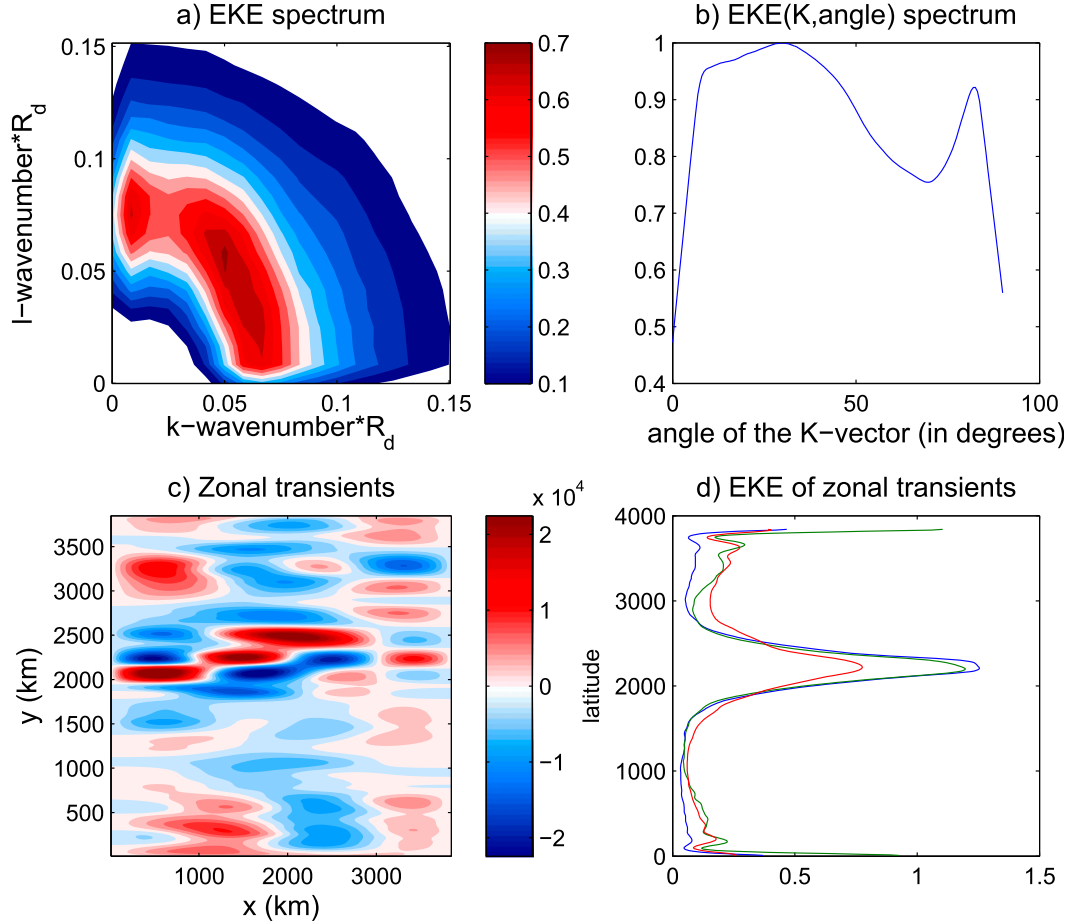


FIG. 2. Spatial structure of the circulation in the numerical simulation. (a) Wavenumber $k-l$ spectrum of velocity in the top layer, time averaged over 50 yr; absolute values of wavenumbers (k, l) are nondimensionalized by R_{d1} ; the spectrum is nondimensionalized by the total kinetic energy (multiplied by 0.005). (b) The spectral power as a function of the angle between the wavenumber (k, l), summed over the interval $K = [1/20R_{d1}, 1/10R_{d1}]$ and divided by its maximum value. Note the presence of the anisotropic peak at small k in (a) and at angle $\approx 85^\circ$ and in (b) corresponding to the zonal transients. (c) Zonal transients, isolated by the low-pass filtering (using the sine transform) of the instantaneous velocity streamfunction in the top layer ($\text{m}^2 \text{s}^{-1}$). (d) Zonally and time-averaged kinetic energy (weighted by the total kinetic energy) of the zonal transients in the three vertical layers.

Zonal transients propagate westward at a speed of approximately $0.035\text{--}0.05 \text{ m s}^{-1}$ north and south of EJE, as estimated from the Hovmöller diagrams. The phase speed of zonal transients is noticeably smaller than the phase speed of the barotropic Rossby wave with the same wavenumbers and in the motionless medium (0.09 m s^{-1}) but are larger than the phase speed of the first baroclinic Rossby wave (0.02 m s^{-1}). This discrepancy is likely to be explained by the effects of the mean advection (Berloff and Kamenkovich 2013a), but the analysis of the normal modes of the double-gyre flow is beyond the scope of this study.

3. Lagrangian analysis

Properties of the eddy-induced material transport are investigated next using Lagrangian particle trajectories. The components of the single-particle dispersion

matrix for a group of N Lagrangian particles are defined as

$$\begin{aligned} D_x(t; x, y) &= \frac{1}{N} \sum_{n=1}^N [x_n(t) - X(t)]^2, \\ D_y(t; x, y) &= \frac{1}{N} \sum_{n=1}^N [y_n(t) - Y(t)]^2, \quad \text{and} \\ D_{xy}(t; x, y) &= \frac{1}{N} \sum_{n=1}^N [x_n(t) - X(t)][y_n(t) - Y(t)], \end{aligned} \quad (5)$$

where x_n and y_n are the zonal and meridional displacements, respectively, of an n th particle from its initial position. The terms X and Y are the ensemble-mean displacements:

$$X(t) = \frac{1}{N} \sum_{n=1}^N x_n(t), \quad Y(t) = \frac{1}{N} \sum_{n=1}^N y_n(t). \quad (6)$$

The dispersion matrix is diagonalized by rotating the coordinate frame, and the angle between the latitude circle and the new x axis θ_{\max} is

$$\tan 2\theta_{\max} = \frac{2D_{xy}}{D_{xx} - D_{yy}}. \quad (7)$$

The rate at which the dispersion in the new coordinate frame (ξ, η) increases with time is used to define the spreading rates:

$$K_\xi(t) = \frac{1}{2} \frac{\partial D_\xi}{\partial t}, \quad K_\eta(t) = \frac{1}{2} \frac{\partial D_\eta}{\partial t}, \quad (8)$$

where

$$D_\xi = D_{xx} \cos^2 \theta + D_{xy} \sin 2\theta + D_{yy} \sin^2 \theta, \\ D_\eta = D_{xx} \sin^2 \theta - D_{xy} \sin 2\theta + D_{yy} \cos^2 \theta. \quad (9)$$

The Lagrangian correlation time scales are calculated (e.g., [Vallis 2006](#)) from the Lagrangian velocity autocorrelation functions R_ξ and R_η in the new coordinate frame:

$$\tau_{\text{corr}}^{(\xi)} = \frac{1}{R_\xi(0)} \int_0^\infty R_\xi(\tau) d\tau, \quad (10)$$

$$\tau_{\text{corr}}^{(\eta)} = \frac{1}{R_\eta(0)} \int_0^\infty R_\eta(\tau) d\tau. \quad (11)$$

The effects of the mean flow on the eddy-induced diffusivity is accounted for by the full trajectory-following (FTF) method ([Berloff et al. 2002](#); [Rypina et al. 2012](#)), which was shown by the latter study to account for such known effects of the mean flow on the eddy diffusivity as the cross-jet suppression of eddy-induced particle spreading and material transport barriers. The method calculates particle dispersion only due to the time-dependent (eddy) part of the flow but along the particle trajectories in the full (eddy plus mean) flow. This effectively captures the effects of the mean advection on the eddy-driven dispersion because the Lagrangian quantities in (1) are determined by particle location. Note that the more straightforward analysis of particles in the full flow cannot serve this purpose because of the particle dispersion by the mean flow itself.

Neutrally buoyant Lagrangian particles are released in 50 consecutive 400-day segments, starting with 130 000 particles in each layer. To examine the spatial distribution of the anisotropic spreading rates, this area is divided into

106 km by 106 km subregions, and the particles are divided into the corresponding groups, according to their initial positions. Particle spreading rates are computed for each subregion over the 400-day time interval. Typically, most particles in each group leave the subregion boundaries before they reach the diffusive regime, and these nonlocal effects must be accounted for. To do this for each group, we define a mean “particle cloud” by its center of mass, using (X, Y) , and by its size, using the average zonal/meridional displacements. If several particle clouds overlap at a given point, the dispersion at this point is estimated by the ensemble average of the corresponding individual cloud dispersions. Particle clouds that touch solid boundaries are discarded.

a. Dispersion regimes

The long time asymptotic behavior of (8) is traditionally used to characterize different dispersion regimes (e.g., [LaCasce 2008](#)). In particular, the diffusive regime corresponds to the linear increase of the dispersion with time, achieved after sufficient time has passed, and (8) then provides an estimate for the eddy diffusivities. Deviations from the diffusion are quantified here by fitting $t^{\alpha+1}$ to $D_\xi(t)$ and $D_\eta(t)$; the corresponding parameters are defined as α_ξ and α_η , respectively. In a purely diffusive regime, α is zero, whereas the superdiffusive regimes correspond to positive and subdiffusive regimes correspond to negative values of this parameter.

The map of parameter α shows that over the 400 days used to estimate the diffusivity in this study, the dispersion is not exactly diffusive in most of the domain ([Fig. 3](#)). In particular, α_ξ and α_η are positive (superdiffusive spreading) in the western part of the domain but are negative (subdiffusive spreading) in the wide region centered around EJE. Spreading tends to become more diffusive in deeper layers. These deviations from the diffusive regime can be explained by several factors. First, the superdiffusive dispersion can be caused by the effects of the persistent shear in velocities. For example, in the extreme case of stationary velocity shear and no eddies, the spreading is purely “ballistic” ($\alpha = 1$). Second, nonzero values of α can be found even in the flow that is locally diffusive but whose eddy kinetic energy and diffusivity vary strongly with location. This can happen because as they spread particles enter regions with weaker (stronger) eddies and thus slow (accelerate) their spreading rates ([Berloff et al. 2002](#); [Rypina et al. 2012](#)); the mean flow can potentially play a dominant role in these effects.

The importance of the mean advection can be estimated here by comparing the dispersion regimes in the control FTF simulation and a more traditional “eddy-only” run, in which the effects of the mean advection are neglected, and the particles only feel (i.e., are advected

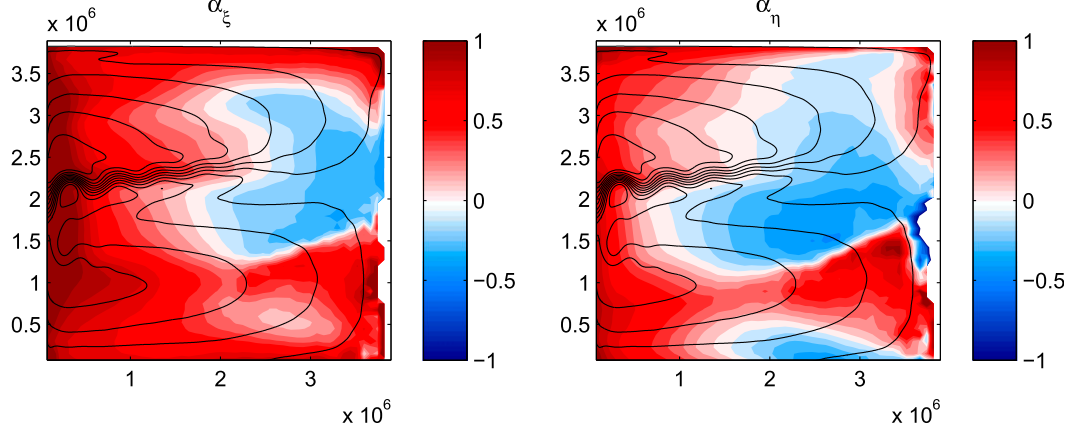


FIG. 3. Spreading regimes in the control simulation. Parameters (left) α_ξ and (right) α_η are shown in the top layer. Positive values correspond to superdiffusive and negative values correspond to subdiffusive spreading.

by) the eddying component of the flow. The eddy-only simulation exhibits more diffusive spreading along the main axis and the basin-averaged magnitude of α_ξ decreases from 0.44 to 0.20. In particular, the particle spreading in the western part of the domain is no longer superdiffusive, and this difference with the control simulation is explained by the mean advection. As particles in the control run move toward EJE, they experience more powerful eddy-driven spreading, which explains the increase in their dispersion and positive values of α_ξ and α_η . These conclusions are consistent with Rypina et al. (2012).

b. Anisotropic dispersion

The eddy diffusivity is strongly anisotropic, with K_ξ exceeding K_η everywhere in the domain (Fig. 4a; Table 1).

The largest diffusivities are found between the gyres in the EJE-dominated part of the domain, where the eddy kinetic energy is also the highest. In the top layer, the anisotropy parameter $a_{\text{aniso}} = K_\xi/K_\eta$ is the largest in the eastern part of the domain, where a_{aniso} reaches 10.0; the area-averaged value of this parameter is 5.2. The spreading is the weakest and most isotropic in the southeastern (northeastern) parts of the subtropical (subpolar) gyres. With depth, the spreading becomes more isotropic near the EJE region but more anisotropic elsewhere (Fig. 4b). This is in accord with a greater relative importance of zonal transients in these regions (section 2). In the area-averaged sense, the anisotropy increases with depth and becomes particularly large in the bottom layer (Table 1). The major dispersion direction is not exactly

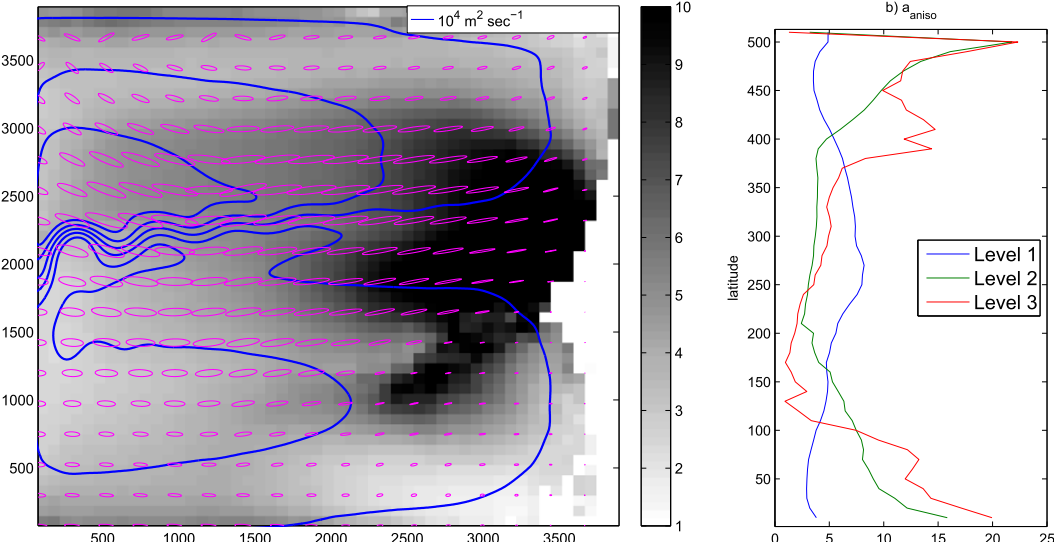


FIG. 4. Anisotropic spreading rates in the control simulation. (left) Spreading ellipses (see text) are superimposed here on the anisotropy parameter a_{aniso} (shaded); every ninth ellipse is shown for presentation purposes. Also shown is the time-mean streamfunction. (right) Zonally averaged a_{aniso} in the three vertical layers.

TABLE 1. Anisotropy coefficient a_{aniso} in four simulations, area averaged within three vertical layers.

		LPx30Rd (zonal transient dominated)	HPx30Rd (isotropic eddy dominated)
Control	EO (no mean advection)		
Level 1	5.2	4.0	7.9
Level 2	6.8	8.4	10.9
Level 3	9.3	11.05	13.7
		2.2	1.8

zonal (area average is approximately 10°) and is therefore not aligned with the f/h contour, where f is the Coriolis frequency and h is the total depth of the fluid. The major spreading direction also crosses the background PV contours, most notably in the east of the domain (Figs. 1c, 4a).

The correlation time scales in the major and minor directions $\tau_{\text{corr}}^{(\xi)}$ and $\tau_{\text{corr}}^{(\eta)}$ exhibit substantial variability in the horizontal and vertical (Table 2), demonstrating that the Lagrangian velocity variance alone is not sufficient to quantify the spatial dependence in diffusivities. The longest time scales are found in the intermediate layer 2 and in the interior of the subpolar and subtropical gyres (away from EJE). The velocity variance cannot explain the anisotropy in diffusivities either since $\tau_{\text{corr}}^{(\xi)}$ substantially exceeds $\tau_{\text{corr}}^{(\eta)}$ in most of the domain. The Lagrangian velocity variance in the major and minor directions $R_\xi(0)$ and $R_\eta(0)$ are, in contrast, very close to each other; the area-averaged ratio between them is 1.05, 1.13, and 0.92 in layers 1, 2, and 3, respectively. This would lead to an erroneous conclusion that diffusivities should be isotropic if the variability in the correlation times is not taken into account. These results are consistent with the analysis of altimetric velocities in Rypina et al. (2012).

c. Causes of the dispersion anisotropy: Mean advection and zonal transients

We first examine the role of the mean advection by comparing the control simulation to the eddy-only (EO) experiment (which was described in section 3a). In the EO simulations, the anisotropy parameter a_{aniso} decreases in the top layer, with the largest changes in the EJE vicinity (not shown). However, a_{aniso} remains larger than 2.0 in most of the domain and is larger than 5 in the northern and southern parts of the domain; the area-averaged value is 4.0. This demonstrates that, even in the absence of mean advection, the eddies cause anisotropic particle spreading. Because of the weakness of the mean advection in the deep layers, the differences between the standard and EO runs are only noticeable in the EJE vicinity. Interestingly, K_η does not increase in the EJE vicinity in response to the removal of the mean advection, which is inconsistent with the idea of cross-flow mixing suppression. It is, however,

TABLE 2. Correlation time scale $\tau_{\text{corr}}^{(\xi)}$ (days) in four simulations within three vertical layers; the reported values are horizontal averages plus or minus the spatial std dev.

		LPx30Rd (zonal transient dominated)	HPx30Rd (isotropic eddy dominated)
Control	EO (no mean advection)		
Level 1	6.5 ± 2.5	8.3 ± 6.1	8.6 ± 3.4
Level 2	17.6 ± 11.4	17.2 ± 10.7	20.5 ± 14.0
Level 3	10.4 ± 3.75	10.6 ± 4.0	15.2 ± 5.7
			6.3 ± 1.8

plausible that our Lagrangian estimates can underestimate the suppression effects by the narrow EJE due to a large size of the corresponding particle clouds.

We next estimate the importance of zonal transients by analyzing a “zonal transient-dominated” sensitivity experiment (Fig. 5a). In this run, we low-pass Fourier filter the velocity streamfunction in the zonal direction with $L_{\text{filter}} = 30R_{d1}$ (simulation LPx30Rd). For this purpose, the flow is decomposed into the Fourier series,¹ all Fourier coefficients corresponding to scales shorter than L_{filter} are set to zero, and the inverse transform is applied. This simulation employs the FTF technique, so the full trajectories of particles are the same as in the control simulation.

The spreading rates become strongly anisotropic with a_{aniso} exceeding 10.0 in most of the domain; a_{aniso} also becomes more spatially uniform. Both K_ξ and K_η are reduced compare to the control run, but the reduction in K_η is particularly dramatic, and this is consistent with the strong reduction in the meridional velocity variance. However, the Lagrangian correlation time scale $\tau_{\text{corr}}^{(\xi)}$ increases, particularly south and north of EJE, and this further outlines the fact that the velocity variance alone cannot explain the anisotropy. Last, the major dispersion direction becomes nearly zonal: the area-averaged θ_{max} increases from only 2° to 4° with depth. These results suggest that zonal transients act to induce primarily zonal material transport and increase the correlation time scale in the major direction.

We now reverse the sensitivity experiment and carry out a simulation in the “isotropic eddy-dominated” experiment (HPx30Rd), where zonal transients are removed from the velocity streamfunction using the high-pass Fourier filter with $L_{\text{filter}} = 30R_{d1}$. Several differences with the control simulation are notable. First, the spreading becomes more isotropic with the area-averaged $a_{\text{aniso}} \approx 2.0$

¹ Note that although the flow satisfies the no-normal flow and no-slip boundary conditions, the streamfunction is not periodic in the strict sense. Nevertheless, the results with the Fourier transform and with and without window tapering and the use of the sine transform lead to very similar results.

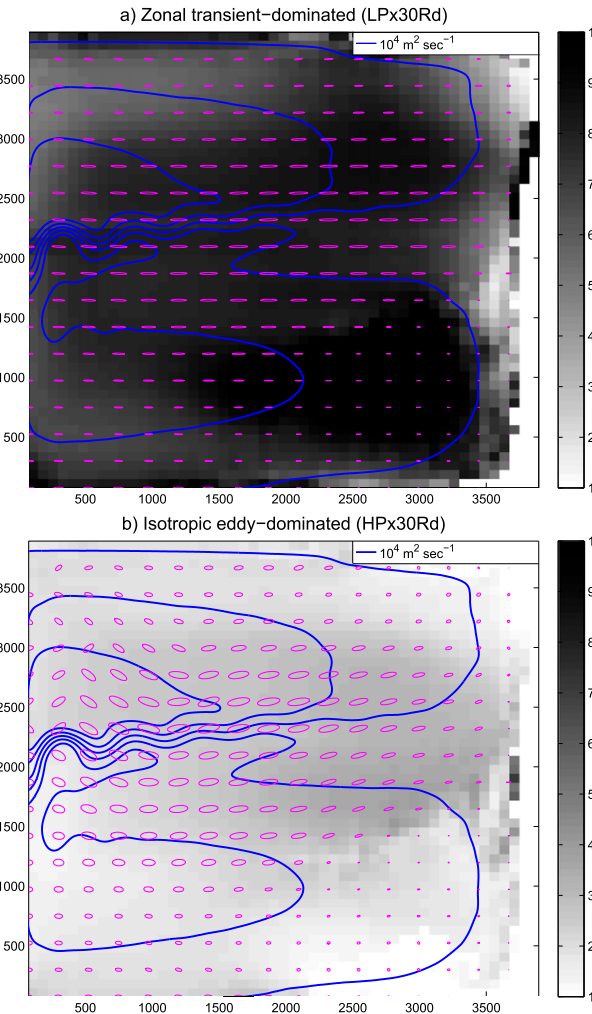


FIG. 5. Sensitivity runs with the Fourier-filtered flows and the importance of zonal transients on the anisotropic spreading rates. (a) Zonal transient-dominated LPx30Rd simulation; (b) isotropic eddy-dominated HPx30Rd simulation. Spreading ellipses (see text) are superimposed here on the anisotropy parameter a_{aniso} (shaded); every ninth ellipse is shown for presentation purposes. Also shown is the time-mean streamfunction.

in all layers. This is despite the fact that $R_\xi(0)$ is generally smaller than $R_\eta(0)$; for example, their area-averaged ratio in the top layer is 0.7. Note that a diffusivity estimate based entirely on the velocity variance would erroneously suggest that particle spreading should become predominantly meridional. Second, the correlation time scale $\tau_{\text{corr}}^{(\xi)}$ is reduced, particularly in layers 2 and 3, and $\tau_{\text{corr}}^{(\eta)}$ is increased, but the difference between these two scales is still significant (Table 3). We can hypothesize that this is explained by the effects of the mean advection and zonal transients on the dispersion by the isotropic eddies, but the exact mechanism needs to be further investigated. Distribution of $\tau_{\text{corr}}^{(\xi)}$ also becomes more

TABLE 3. Correlation time scale $\tau_{\text{corr}}^{(n)}$ (days) in four simulations within three vertical layers; the reported values are horizontal averages plus or minus the spatial std dev.

	EO (no mean advection)	LPx30Rd (zonal transient dominated)	HPx30Rd (isotropic eddy dominated)
Control			
Level 1	2.0 ± 1.5	3.7 ± 2.6	11.7 ± 5.0
Level 2	3.7 ± 2.4	3.4 ± 2.5	13.1 ± 5.4
Level 3	1.8 ± 1.2	1.8 ± 1.5	5.9 ± 2.0
			2.5 ± 1.5

spatially uniform (Table 2), which suggests that the velocity variance can be more readily used to quantify eddy diffusivity. Third, the direction of the maximum spreading is more nonzonal than in the control run, and the area-averaged $\theta_{\text{max}} \approx 16^\circ$. These results demonstrate that the isotropic eddies induce weakly anisotropic transport, with more spatially uniform correlation scales.

4. Anisotropic transport and its causes in altimetry-based estimates

The model-based results in section 3 strongly indicate that the anisotropy of the eddy-induced material transport and the predominantly zonal direction of preferred particle spreading are largely controlled by zonal transients. We now test these conclusions using a 17-yr-long record (from 1992 to 2009) of the geostrophic velocities inferred from AVISO sea surface height altimetric measurements. We focus here on the subtropical North Atlantic from 20° to 50°N and from 70° to 20°W ; the data and methods are the same as in Rypina et al. (2012). Similar to the model-based $k-l$ velocity spectrum shown in Fig. 2, the spectrum of geostrophic velocities (Fig. 6) contains a noticeable peak in its zonal transient portion, where zonal scales exceed 1000 km. Unlike the model results, however, the isotropic part of the spectrum contains multiple peaks.

We now investigate the influence of this zonal transient spectral peak on the eddy-induced diffusivity by comparing particle spreading in simulations with the unfiltered eddies (control run) to simulations with the low-pass filtered (zonal transient dominated) and high-pass filtered (isotropic eddy dominated) eddy fields. As before, the diffusivities are quantified using the FTF approach and are visualized using the diffusivity ellipses (Fig. 7). In comparison to the control run (green ellipses), in the zonal transient-dominated simulations (blue ellipses) both the zonal and meridional components of diffusivity become smaller, but the meridional component decreases significantly more than the zonal component. As a result, the ellipses become nearly zonal throughout most of the domain, and the anisotropy coefficient increases from 5.4 in the control to 7.9 in the zonal

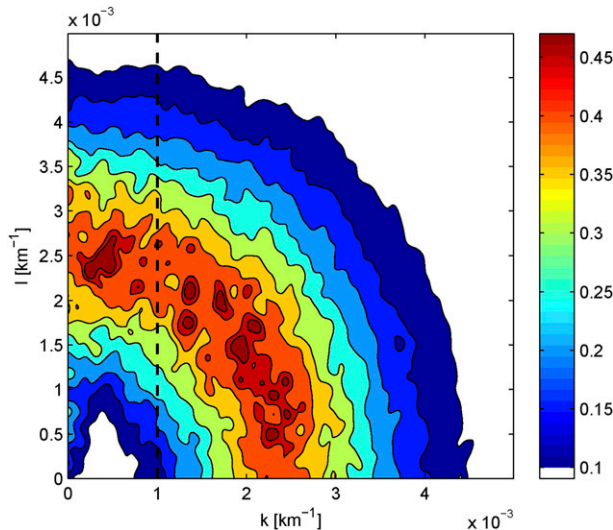


FIG. 6. Spatial ($k-l$) velocity spectrum of the geostrophic velocity (sum of the u and v velocity spectra, where u and v are in km day^{-1}) inferred from the AVISO satellite altimetry, time averaged over the period from 1992 to 2009.

transient-dominated run. If, in the opposite, zonal transients are removed in the isotropic eddy-dominated flow, the zonal component of diffusivity decreases more than the meridional, and the ellipses become less anisotropic with the domain-averaged anisotropy coefficient of only 2.5 (Fig. 7, bottom). All of these results are in agreement with the model-based results of section 3.

5. Tracer distribution in the numerical model

A practical application of the diffusivity estimates is to use them to parameterize eddies in non-eddy-resolving simulations. The task of eddy parameterization is therefore to reproduce tracer distribution using the diffusion instead of the eddy advection. We test the validity of this approach in simulations with idealized tracer release experiments. The distribution of the tracer $c(x, y, t)$ is governed by the standard advective-diffusive equation:

$$\frac{\partial c}{\partial t} + \mathbf{u} \cdot \nabla c = \nabla \cdot \mathbf{K} \nabla c + k_{\text{bh}} \nabla^2 \nabla^2 c + F, \quad (12)$$

where \mathbf{K} is the diffusivity tensor estimated using

$$\mathbf{K} = \begin{pmatrix} K_x & K_{xy} \\ K_{xy} & K_y \end{pmatrix} = \frac{1}{2} \frac{\partial}{\partial t} \begin{pmatrix} D_{xx} & D_{xy} \\ D_{xy} & D_{yy} \end{pmatrix}, \quad (13)$$

and k_{bh} is the biharmonic diffusivity required for numerical stability; its value of $-5 \times 10^{10} \text{ m}^4 \text{ s}^{-1}$ is the same in all simulations. The term $F(x, y)$ is the tracer source/sink.

We consider evolution of an isolated tracer patch:

$$c(x, y, 0) = \exp \left[- \left(\frac{x - x_0}{s_x} \right)^2 - \left(\frac{y - y_0}{s_y} \right)^2 \right], \quad (14)$$

where (x_0, y_0) defines a center of the patch, and s_x and s_y is the size of the patch. We initialize the model with three tracer release experiments: a patch centered around EJE (central patch), a patch south of EJE (southern patch), and a patch north of EJE (northern patch).

In the absence of eddies, each patch is assumed to be balanced by a constant tracer source F :

$$F(x, y) = \bar{\mathbf{u}} \cdot \nabla c(x, y, 0) - k_{\text{bh}} \nabla^2 \nabla^2 c(x, y, 0), \quad (15)$$

where $\bar{\mathbf{u}}$ is the time-mean velocity. We, therefore, consider a tracer anomaly that is due to a steady source, and this situation is relevant to tracers that do not have a direct feedback on their sources (such as surface salinity). The particular shape of (15) also corrects for the direct effects of the mean advection on the initial patch, which simplifies a comparison to the Lagrangian studies in section 3. Simulations with $F = 0$ were also carried out and led to qualitatively similar conclusions, although the quantitative analysis is more challenging because of the significant deformation of the patches by the mean advection, collision of the patches with solid walls, and entrainment of the tracer into the western boundary current and EJE. It is, however, important to note that the mean advection is not powerful enough to dwarf the effects of eddies even if $F = 0$ and the tracer distributions with and without eddies are substantially different within the subtropical and subpolar gyre regions (Fig. 8). This demonstrates the importance of the eddy advection even in the along-mean flow direction; if the opposite were true, only cross-mean flow diffusivity would be important and the anisotropic tensor \mathbf{K} would not have any practical significance.

In the control simulation, the tracer is advected by the full flow (mean and eddy) and $\mathbf{K} = 0$. Ten consecutive 400-day simulations are averaged for the analysis. By the day 200, the patches are substantially modified by the eddying flow (Fig. 9); the deformation is much stronger at day 400, which complicates the analysis at later stages. The integration is not continued beyond day 400 despite the fact that the statistical steady state is not reached. The southern and northern patches are being dispersed by eddies, whereas their centers of mass are moving very little in all simulations because of the action of F . The center of mass of the central patch in the top layer, in contrast, moves northwest despite the action of F ; the distortion of the patch is still significantly smaller than in the $F = 0$ simulation. Layers 2 and 3 and all parameterized runs described below do not have the same problem.

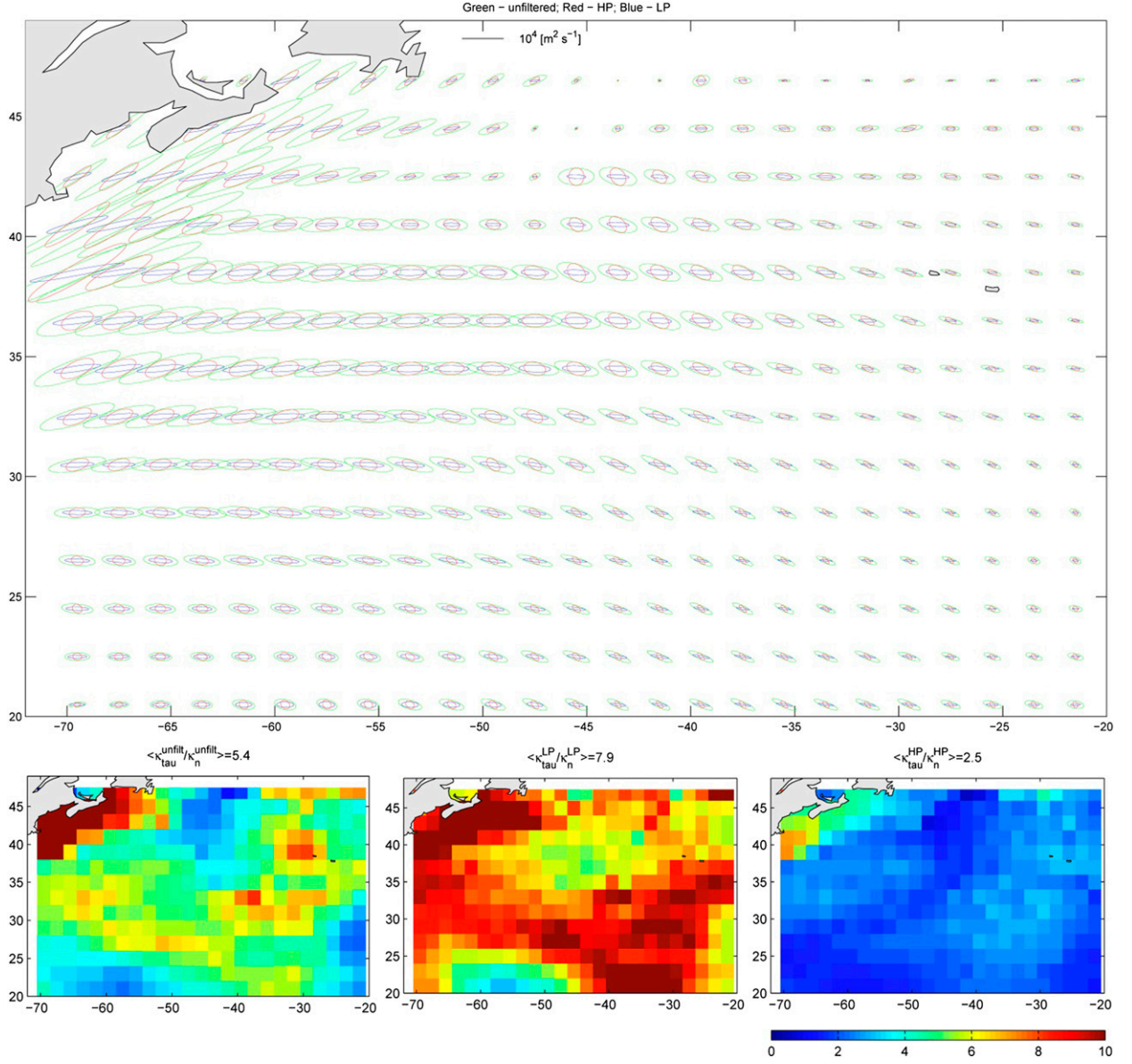


FIG. 7. Anisotropic transport and its causes in altimetry-based estimates of North Atlantic circulation. (top) Diffusivity ellipses in the three simulations: full unfiltered flow (green), low-pass filtered zonal transient-dominated flow (blue), and high-pass filtered flow (red). Anisotropy parameter a_{aniso} in three simulations: (bottom left) full unfiltered flow, (bottom middle) low-pass filtered flow, and (bottom right) high-pass filtered flow.

We next analyze a series of sensitivity simulations, in which a part of the eddying flow is removed and replaced with diffusion. The resulting errors are quantified by the mean square of the difference with the control simulation for each patch; to make these numbers more meaningful, we also divide them by the mean square changes in the control simulation (Table 4):

$$C_e = \langle [c(x, y, t) - c_{\text{control}}(x, y, t)]^2 \rangle \times \langle [c_{\text{control}}(x, y, t) - c_{\text{control}}(x, y, 0)]^2 \rangle^{-1},$$

where the angular brackets stand for the spatial average, and c_{control} is the tracer concentration in the control simulation. One needs to recall that the task of diffusion-based parameterization is to reproduce large-scale fields of the control simulation. To prevent the small-scale variance from dominating the errors and to make the quantitative analysis more relevant to the task of parameterization, the tracer is smoothed with a running-mean spatial filter with a width of 112 km (15 grid points).

The eddy velocities are removed and replaced with $\mathbf{K}(x, y)$ estimated using (13) from the data of section 3.

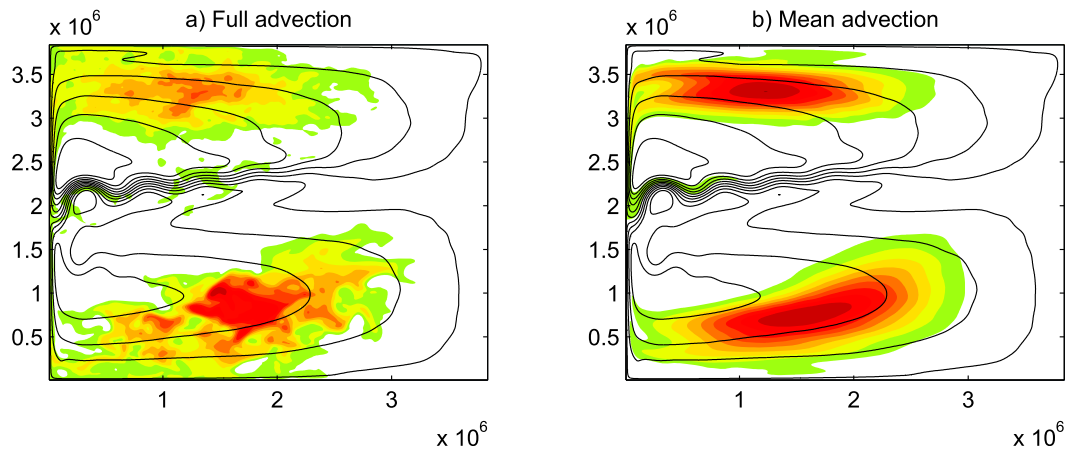


FIG. 8. Importance of eddies in the idealized tracer distributions. Tracer concentrations are shown at day 100 for two simulations with $F = 0$ and (a) full flow and (b) mean advection only. Central patch release is not shown because of its strong deformation by the EJE. Time-mean streamlines are shown by the black contours.

The resulting tracer distributions are similar to the control simulation in terms of the path location and shape, including eastward displacement of the center of the northern patch, small westward displacement of the center of the central patch, and asymmetric deformation of the southern patch (Fig. 9). There are also some noticeable differences. In addition to the tracer distribution being considerably smoother than in the control simulation (which is expected), tracer maxima in the middle of each patch are also smeared out, and the meridional dispersion is generally overestimated. The largest differences are in the central and southern patches (Table 4). All these biases can be attributed to the nonuniform distribution of eddy diffusivity, nonlocal Lagrangian methods used to estimate \mathbf{K} , and nondiffusive particle spreading.

What is the relative importance of zonal transients and isotropic eddies? To answer this question, we carried out the zonal transient-dominated simulation with LPx30Rd velocities and isotropic eddy-dominated simulation with HPx30Rd velocities. Both simulations have $\mathbf{K} = 0$. The isotropic eddy-dominated simulation is intended to estimate the importance of zonal transients by removing their effects from the control run. The flow in this run contains most of the eddy fields (everything except zonal transients), and the improvements over the simulation with $\mathbf{K}(x, y)$ can be anticipated and are indeed observed in layer 1 and central patches in all layers. Nevertheless, the absence of zonal transients causes considerable biases, most notably in the southern patch, which is overly symmetric in this simulation.

The effects of zonal transients are further studied in the zonal transient-dominated run. Simulated tracer distributions are surprisingly close to the simulation with $\mathbf{K}(x, y)$ and even show some noticeable improvements, particularly for the southern patch and in layer 3. This is

despite the fact that a rather small portion of the eddying velocities is used to advect the tracer. Tracer simulation with explicit zonal transients can be further improved if additional mixing is introduced to compensate for the missing isotropic eddies. To show the potential for such improvement, we add a constant isotropic diffusion with constant $K = 500 \text{ m}^2 \text{ s}^{-1}$. This is a rather typical value for isopycnal diffusivities in coarse resolution models, but it is smaller than the area-averaged values of K_ξ and K_η in the control simulation in the top two layers. Values of 250 and $1000 \text{ m}^2 \text{ s}^{-1}$ have also been tried but led to very similar values of C_e . In comparison to both the simulations with $K(x, y)$ and isotropic eddies, this run exhibits noticeable improvements everywhere, except in the central patch of the top layer. Clearly, an explicit simulation of zonal transients has a pronounced effect on tracer simulations, and the parameterization of the eddy transport seems more plausible in this case.

6. Discussion and conclusions

This study examines the anisotropic transport properties of the eddying North Atlantic flow, using an idealized model of the double-gyre oceanic circulation and altimetry-derived velocities. In this study, we decompose the flow into three main components: time-mean advection, large-scale zonal transients, and the remainder of the eddy field. The material transport by the time-dependent flow (quantified by the eddy diffusivity tensor) varies geographically and is anisotropic, that is, it has a well-defined direction of the maximum transport. These properties are primarily explained by the action of transient motions, rather than the effects of the time-mean advection. In particular, zonal transients correspond to the primarily zonal material transport and explain the

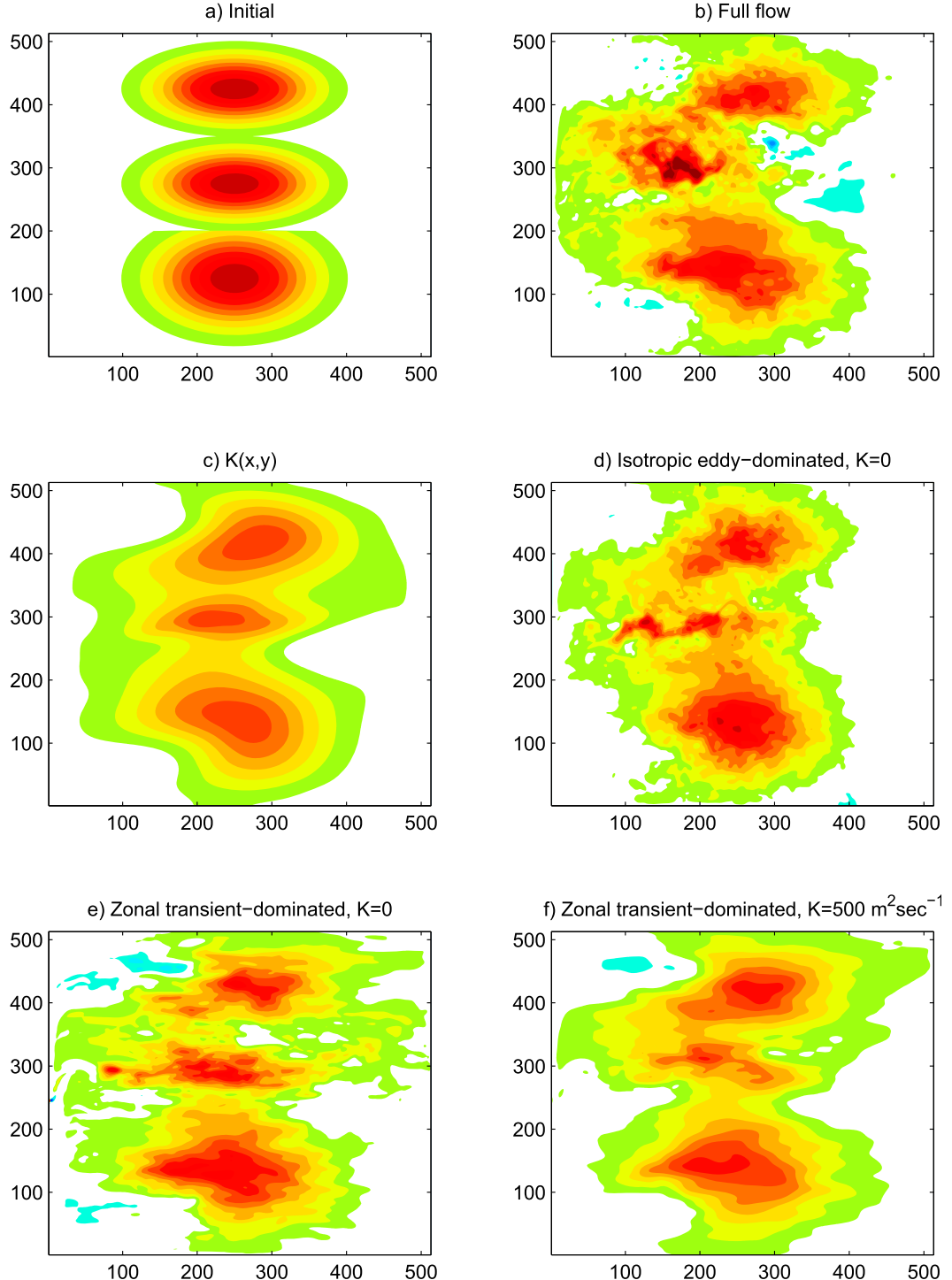


FIG. 9. Distribution of an idealized tracer in numerical simulations. Tracer patches from the three different releases (northern patch, central patch, and southern patch) are overlapped and shown (in the top layer at day 200) for the initial distribution and sensitivity experiments.

largest part of anisotropy in diffusivities for both numerically simulated and altimetry-based velocity fields.

Zonal transients are defined using the spatial velocity spectrum, which, in the upper ocean, shows a peak at the

basinwide zonal scale and a nearly meridional wavevector. Because of these spectral properties, Lagrangian velocities in zonal transient-dominated flows are predominantly zonal and have persistent correlations in

TABLE 4. Weighted mean square error in the tracer concentration (see text) at day 200 shown for the three tracer patches and in the three vertical layers.

		$K(x, y)$	Zonal-transient dominated ($K = 0$)	Isotropic-eddy dominated	Zonal-transient dominated ($K = 500$)
Level 1	North	0.18	0.30	0.18	0.22
	Center	0.46	0.42	0.25	0.36
	South	0.41	0.21	0.33	0.18
Level 2	North	0.13	0.24	0.18	0.08
	Center	0.20	0.30	0.165	0.12
	South	0.34	0.15	0.33	0.14
Level 3	North	0.57	0.33	0.43	0.25
	Center	1.71	0.29	0.16	0.43
	South	0.435	0.23	0.37	0.37

time. This makes zonal transients a particularly effective vehicle for the anisotropic material transport, despite the fact that the amount of energy contained in the zonal transient portion of the spectrum is relatively small. Anisotropy in transport is due primarily to the difference in the correlation time scales, rather than anisotropy of the velocity covariance matrix. Our definition of these transients is based solely on their zonal scales and they are, strictly speaking, spectral Fourier modes in the zonal direction. The dynamical interpretation of these transients and their origins remains to be established. In particular, it is possible that zonal transients are normal modes and exist because of the linear dynamics through their interactions with the mean flow (Berloff and Kamenkovich 2013a,b). Alternatively, the energy at the zonal transient part of the spectrum can exist because of the nonlinear energy transfer due to interactions among transient eddies (Arbic et al. 2014). Investigation of the dynamics of zonal transients is left for future studies.

Anisotropy in transport is quantified here using a diagonalized diffusivity tensor, although the transport properties are almost never perfectly diffusive. This nondiffusive behavior, combined with spatial inhomogeneity and anisotropy, makes the parameterization of eddy-induced transport challenging. This is demonstrated by biases in idealized tracer distributions in simulations, in which the eddy-induced transport is parameterized using Lagrangian diffusivity estimates. Since such estimates are not globally available below the surface, finding an effective parameterization for the entire eddying flow may be even more difficult than our study implies. Our results suggest, however, that this task becomes easier in simulations with explicit zonal transients since these flow components are associated with a large part of the complexity in the transport, such as spatial variability in the decorrelation scales and anisotropy. Zonal transients are large enough to be resolved by most numerical simulations even at relatively coarse spatial resolution, but such non-mesoscale-resolving simulations may lack the dynamics necessary to simulate

zonal transients. The importance of large-scale transients and the utility of the Lagrangian estimates of eddy diffusivity need to be further studied for more realistic, climatically relevant tracers. This can be done using simulations with and without eddy advection (as in Booth and Kamenkovich 2008) and will be a subject of a future study.

Acknowledgments. We thank two anonymous reviewers for their helpful suggestions on improving this manuscript. IK would like to acknowledge support through the NSF Grant OCE-1154923. IR was supported by the NSF OCE-1154641 and NASA Grant NNX14AH29G.

REFERENCES

Arbic, B., M. Mueller, J. Richman, J. Shriner, A. Morten, R. Scott, G. Serazin, and T. Penduff, 2014: Geostrophic turbulence in the frequency-wavenumber domain: Eddy-driven low-frequency variability. *J. Phys. Oceanogr.*, **44**, 2050–2069, doi:10.1175/JPO-D-13-054.1.

Berloff, P., and I. Kamenkovich, 2013a: On spectral analysis of mesoscale eddies. Part I: Linear analysis. *J. Phys. Oceanogr.*, **43**, 2505–2527, doi:10.1175/JPO-D-12-0232.1.

—, and —, 2013b: On spectral analysis of mesoscale eddies. Part II: Nonlinear analysis. *J. Phys. Oceanogr.*, **43**, 2528–2544, doi:10.1175/JPO-D-12-0233.1.

—, J. C. McWilliams, and A. Bracco, 2002: Material transport in oceanic gyres. Part I: Phenomenology. *J. Phys. Oceanogr.*, **32**, 764–796, doi:10.1175/1520-0485(2002)032<0764:MTIOGP>2.0.CO;2.

—, I. Kamenkovich, and J. Pedlosky, 2009: A mechanism for the formation of multiple zonal jets in the oceans. *J. Fluid Mech.*, **628**, 395–425, doi:10.1017/S0022112009006375.

Booth, J., and I. Kamenkovich, 2008: Isolating the role of mesoscale eddies in mixing of a passive tracer in an eddy resolving model. *J. Geophys. Res.*, **113**, C05021, doi:10.1029/2007JC004510.

Ferrari, R., and M. Nikurashin, 2010: Suppression of eddy diffusivity across jets in the Southern Ocean. *J. Phys. Oceanogr.*, **40**, 1501–1519, doi:10.1175/2010JPO4278.1.

Freeland, H. J., P. B. Rhines, and T. Rossby, 1975: Statistical observations of the trajectories of neutrally buoyant floats in the North Atlantic. *J. Mar. Res.*, **33**, 383–404.

Green, J. S. A., 1970: Transfer properties of the large-scale eddies and the general circulation of the atmosphere. *Quart. J. Roy. Meteor. Soc.*, **96**, 157–185, doi:10.1002/qj.49709640802.

Haynes, P. H., D. A. Poet, and E. F. Shuckburgh, 2007: Transport and mixing in kinematic and dynamically consistent flows. *J. Atmos. Sci.*, **64**, 3640–3651, doi:10.1175/JAS4030.1.

Henning, C. C., and G. Vallis, 2004: The effects of mesoscale eddies on the main subtropical thermocline. *J. Phys. Oceanogr.*, **34**, 2428–2443, doi:10.1175/JPO2639.1.

Huang, H.-P., A. Kaplan, E. Curchitser, and N. Maximenko, 2007: The degree of anisotropy for mid-ocean currents from satellite observations and an eddy-permitting model simulation. *J. Geophys. Res.*, **112**, C09005, doi:10.1029/2007JC004105.

Kamenkovich, I., P. Berloff, and J. Pedlosky, 2009: Anisotropic material transport by eddies and eddy-driven currents in a model of the North Atlantic. *J. Phys. Oceanogr.*, **39**, 3162–3175, doi:10.1175/2009JPO4239.1.

Karabasov, S. A., P. S. Berloff, and V. M. Goloviznin, 2009: CABARET in the ocean gyres. *Ocean Modell.*, **30**, 155–168, doi:10.1016/j.ocemod.2009.06.009.

Killworth, P., 1997: On the parameterization of the eddy transfer. Part I. Theory. *J. Mar. Res.*, **55**, 1171–1197, doi:10.1357/0022240973224102.

LaCasce, J. H., 2000: Floats and f/H. *J. Mar. Res.*, **58**, 61–95, doi:10.1357/002224000321511205.

—, 2008: Lagrangian statistics from oceanic and atmospheric observations. *Transport and Mixing in Geophysical Flows*, J. B. Weiss and A. Provezale, Eds., Springer, 165–228.

—, and A. Bower, 2000: Relative dispersion in the subsurface North Atlantic. *J. Mar. Res.*, **58**, 863–894, doi:10.1357/002224000763485737.

Prandtl, L., 1925: Bericht über Untersuchungen zur ausgebildeten Turbulenz. *Z. Angew. Math. Mech.*, **5**, 136–139.

Rypina, I. I., L. J. Pratt, and M. S. Lozier, 2011: Near-surface transport pathways in the North Atlantic Ocean: Looking for throughput from the subtropical to subpolar gyre. *J. Phys. Oceanogr.*, **41**, 911–925, doi:10.1175/2011JPO4498.1.

—, I. Kamenkovich, P. Berloff, and L. Pratt, 2012: Eddy-induced particle dispersion in the near-surface North Atlantic. *J. Phys. Oceanogr.*, **42**, 2206–2228, doi:10.1175/JPO-D-11-0191.1.

Sallee, J.-B., K. Speer, R. Morrow, and R. Lumpkin, 2008: An estimate of Lagrangian eddy statistics and diffusion in the mixed layer of the Southern Ocean. *J. Mar. Res.*, **66**, 441–463, doi:10.1357/002224008787157458.

Samelson, R., 1992: Fluid exchange across a meandering jet. *J. Phys. Oceanogr.*, **22**, 431–444, doi:10.1175/1520-0485(1992)022<0431:FEAAMJ>2.0.CO;2.

Smith, K. S., 2005: Tracer transport along and across coherent jets in two-dimensional turbulent flow. *J. Fluid Mech.*, **544**, 133–142, doi:10.1017/S0022112005006750.

Spall, M. A., P. L. Richardson, and J. Price, 1993: Advection and eddy mixing in the Mediterranean salt tongue. *J. Mar. Res.*, **51**, 797–818, doi:10.1357/0022240933223882.

Taylor, G. I., 1921: Diffusion by continuous movements. *Proc. London Math. Soc.*, **20**, 196–211, doi:10.1112/plms/s2-20.1.196.

—, 1953: Dispersion of soluble matter in solvent flowing slowly through a tube. *Proc. Roy. Soc. London*, **A219**, 186–203, doi:10.1098/rspa.1953.0139.

Vallis, G. K., 2006: *Atmospheric and Oceanic Fluid Dynamics*. Cambridge University Press, 745 pp.

Veneziani, M., A. Griffa, A. M. Reynolds, Z. D. Garraffo, and E. P. Chassignet, 2005: Parameterizations of Lagrangian spin statistics and particle dispersion in the presence of coherent vortices. *J. Mar. Res.*, **63**, 1057–1083, doi:10.1357/002224005775247571.

Young, W. R., P. B. Rhines, and C. J. R. Garrett, 1982: Shear-flow dispersion, internal waves and horizontal mixing in the oceans. *J. Phys. Oceanogr.*, **12**, 515–527, doi:10.1175/1520-0485(1982)012<0515:SFIDIWA>2.0.CO;2.